Solid Earth Discuss., 4, 1165–1204, 2012
www.solid-earth-discuss.net/4/1165/2012/
doi:10.5194/sed-4-1165-2012

Solid Earth Discussions

Strain localisation in mechanically Layered Rocks, insights from numerical modelling

L. Le Pourhiet[1,2], B. Huet[3], P. Agard[1,2], L. Labrousse[1,2], L. Jolivet[4], and K. Yao[5]

[1]UPMC Univ Paris 06, UMR 7193, ISTEP, 75005, Paris, France
[2]CNRS, UMR 7193, ISTEP, 75005, Paris, France
[3]Department for Geodynamics and Sedimentology, University of Vienna, Althanstrasse 14 1090 Vienna
[4]ISTO, UMR CNRS 6113, Université d'Orléans, Campus CNRS, 1A rue de La Férollerie, 45071 Orléans Cedex, France
[5]Mines ParisTech, Centre de Géosciences, 35 rue Saint Honoré, 77305 Fontainebleau, France

Received: 10 August 2012 – Accepted: 14 August 2012 – Published: 5 September 2012

Correspondence to: L. Le Pourhiet (laetitia.le_pourhiet@upmc.fr)

Published by Copernicus Publications on behalf of the European Geosciences Union.

Abstract

Small scale deformation in stratified rocks displays a large diversity of micro-structures, from the microscopic scale to the scale of orogens. We have designed a series of fully dynamic numerical simulations aimed at assessing which parameters control this structural diversity and which underlying mechanisms lead to strain localisation. The influence of stratification orientation on the occurrence and mode of strain localisation is tested by varying the initial dip of inherited layering versus the large scale imposed simple shear. The detailed study of the models indicates that (1) the results are length-scale independent, (2) the new shear zones are always compatible with the kinematics imposed at the boundary (3) micro-structures formed encompass the full diversity of micro-structures observed in the field and chiefly depend on the direction of the initial anisotropy versus shear direction, (4) depending on the orientation of the anisotropy, the layers may deform along subtractive or additive shear bands, (5) the deformation in anisotropic media results in non-lithostatic pressure values that are on the order of the deviatoric stress in the strong layers and (6) the introduction of brittle rheology is necessary to form localised shear bands in the ductile regime.

1 Introduction

Mechanical layering is present at all scale in rocks as a results of sedimentation, diagenesis, inherited strain (nappe stacking, folding, foliation, schistosity), intrusion of magmatic bodies. Shear localisation in these layered media results in strain partitioning between high strain domains shear bands or kink bands and low strain domains where the initial layering (Sn) is deflected but preserved. The scale of these structures ranges from grain size (hundreds of μm) up to hundreds of km (Hippertt, 1999). These structures constitute a classical tool to reconstruct the kinematics of the deformation (Simpson and Schmid, 1983; Hanmer and Passchier, 1991). Based on a representative set of measurements, it allows one to upscale the field observations to

SED
4, 1165–1204, 2012

larger scale kinematics and draw conceptual geodynamic models at the plate boundary scale; e.g. Cloos (1946); Ramsay (1980); Choukroune et al. (1987); Cosgrove (2007). Kinematic models based on flow partitioning related to the layering of the media (Platt, 1984; Platt and Vissers, 1980; Lister and Williams, 1983; Michibayashi and Murakami, 2007) lead to non-unique solutions because strain consists of more independent components than kinematic constraints allow to solve for. As a result, several kinematic models may be proposed to explain the same finite deformation (Carreras, 2001). The only solution to recover the full dynamics of the system with a unique solution is to introduce rheological relationships in order to compute the complete stress/strain evolution.

As it was shown by Cobbold et al. (1971), models with alternating stiff and weak isotropic viscous layers displays an effective anisotropic behaviour at larger scale allowing the formation of kink bands or shear bands depending on the orientation of the initial layering orientation. The orientations of these bands are successfully reproduced by mathematical models based on linear stability analysis established for anisotropic media (Biot, 1964; Cosgrove, 1976), which are yet applicable only for very small strain and peculiar orientation of the initial layering versus the maximum compressive stress σ_1. Attempts have been made to numerically model large strain in anisotropic media (Muhlhaus et al., 2002, 2004). These studies were focusing on folding and mantle convection. The main results were that anisotropy enhances the shear instabilities. Small scale perturbations of the anisotropy compared to the layer thickness favoured the growth of mullions over folds, which develop for larger scale perturbations (Muhlhaus et al., 2002). However, models using anisotropic constitutive laws rather than a layered media have the disadvantage not to provide any physical length-scale.

Following previous studies (Mancktelow, 2006; Frehner et al., 2011), we make use of numerical codes that the momentum equation for stress and strain to perform dynamic numerical models of previously stratified rocks. The paper concentrates on the impact of a pre-existing layering on the occurrence, the dynamics and the preferred orientations of new localised band of deformation and new flattening planes in medium (10 m)

SED
4, 1165–1204, 2012

to large scale (1 km) shear zones deforming in a regime which is closed to the brittle ductile transition. As Mancktelow (2006) showed plastic yielding was an important parameter for localisation, we introduce a maximum yield strength using morh coulomb rheology (Vermeer and De Borst, 1984; Le Pourhiet, accepted). Exhumed examples of such shear zones are described in all geodynamic settings (compression e.g. Alps (Handy et al., 2005), extension eg Betics (Platt and Vissers, 1980) Aegean(Jolivet et al., 2010), strike-slip e.g. red river fault (Leloup et al., 1995), cap de creus spain (Fusseis et al., 2006)). Based on the example of the western Gulf of Corinth (Greece), where an active basal detachment zone is suspected to accommodate the extension at around 10–15 km depth, the models use a reference shear rate of $1\,cm\,yr^{-1}$ distributed over 1 km thick zone (Avallone et al., 2004) and a confining pressure of 400 MPa (intended to simulate a shear zone buried at 15 km depth). In these conditions, the background strain rate approaches $3\,10^{-13}\,s^{-1}$ and brittle ductile interaction are expected to occurs for effective viscosity as low as $10^{20}\,Pa\,s^{-1}$.

After describing the model set up, we describes how varying the orientation of the layering versus the bulk shear direction may enhance or retard strain localisation and how the layering controls the orientation of the new localised shear zones when they occurs. The modelling results are analysed in term of finite strain, evolution of pressure and deviatoric stresses in the strong and weak layer of the system with shear localisation. In a second part, we fix the orientation of the layering versus shear direction for a case that strongly favour shear localisation in order to study in details the impact of length scale, effective viscosity contrast, plasticity, and strain rate on the degree of localisation.

SED
4, 1165–1204, 2012

2 Influence of the initial orientation on the deformation pattern

2.1 Model set up

The mechanical anisotropy is introduced following the approach of Cobbold et al. (1971) rather than modelling true anisotropic media in order to impose a length scale that overrides the one of the numerical mesh but still allows the formation of several localised band in the models. Numerical experiments allow modelling background strains of the order of 100 %. We focus the quantitative analysis on large strain simple shear numerical experiments using fully visco-elasto-plastic rheology. We present the large panel of micro structures that can form for different degrees of obliquity between the main anisotropic direction and the shear direction. The description of these structures is accompanied by the measure of the large scale softening or hardening associated to their formation. This complements the pre-existing linear stability analysis approach since the numerical simulation are run for larger strain and for orientations which are not initially aligned with the instantaneous stretching and shortening axes.

Therefore most of the simulations are done at a given 4×1 km scale with viscosities that are believed to be close to those at the top of the ductile crust, i.e. 10^{19} and 10^{21} Pa s^{-1} for the weak and strong layers respectively. has been chosen in accordance with

The initial dip δ_0 of the layers Sn (Fig. 1a) is counted positive when they dips towards the right of the model. The models have a large aspect ratio to avoid the impact of boundary conditions. The grey and white layers on Fig. 1a represent the alternance of low and high viscosity layers. Each layer is 30 m thick and corresponds to 3 elements. Boundary conditions correspond to simple shear simulating an infinitely long body by fixing the velocity as parallel to the direction of shearing on the lateral boundary. The vertical gradient of horizontal velocity is constant on the lateral boundaries to simulate large scale simple shear at the scale of the model. Throughout the paper, the intensity of bulk shear strain γ^{bulk} is given in % and corresponds to the tangent of the angle γ on Fig. 1a. Horizontal velocity varies from 0.5 cm yr^{-1} to the left at the top of the model to

SED
4, 1165–1204, 2012

–0.5 cm yr^{-1} to the right at the bottom (Fig. 1b). To avoid the impact of lateral boundary conditions, the results shown correspond to portions located at the center and top of the simulations (see the grey and white boxes in Fig. 1b).

We have deliberately simplified the problem by removing gravity and temperature dependance of viscosity from the model to keep the problem general and independent from the orientation of the shear direction versus gravity and thermal gradients. All the layers have the same visco-elasto-plastic rheology with only viscosity varied and the code approximates the solution of the momentum equilibrium using a mesh of 400 × 100 elements. The conservation equation relates the change of volume to the pressure via the elastic compressibility of the media. Internal friction angle (ϕ) is set to 30°, cohesion (C_0) to 20 MPa, the elastic bulk (K) and shear (G) moduli are respectively set to 50 and 30 GPa.

At γ^{bulk} = 100 %, a large range of microstructures can form depending on the original orientation δ_0 of the layering. They include symmetric boudins, asymmetric boundins, true S-C structures and symmetric folds or kink folds (Fig. 3). Type I and II correspond to positive values of δ_o and include the models in which the strong layers are initialy stretched. They have been separated based on the predominance of shear bands in the type II models. Types III and IV correspond to models in which the initial foliation shortens initially ($\delta_o < 0$). They have been separated based on whether the deformed initial layering (Sn) is being tilted towards positive values of δ during the simulation (Type IV) or not (Type III).

2.2 Results at one glance

At γ^{bulk} = 100%, a large range of microstructures can form depending on the original orientation δ_0 of the layering. They include symmetric boudins, asymmetric boundins, true S-C structures and symmetric folds or kink folds (Fig. 3). Type I and II correspond to positive values of δ_o and include the models in which the strong layers are initialy stretched. They have been separated based on the predominance of shear bands in

SED
4, 1165–1204, 2012

the type II models. Types III and IV correspond to models in which the initial foliation shortens initially ($\delta_o < 0$). They have been separated based on whether the deformed initial layering (Sn) is being tilted towards positive values of δ during the simulation (Type IV) or not (Type III). When $|\delta_0| < 30^\circ$ (Type I and III), the shear strain primarily occurs in the weak layers of the pre-existing foliation. However, secondary structures begin to appear as soon as an initial obliquity of $|\delta_0| = 20^\circ$ is reached, whilst an obliquity of $|\delta_0| = 40^\circ$ is needed for true S-C structures to develop. When shear bands form, they do not form parallel to the direction of shear except for the special $\delta_0 = 45^\circ$ case. The dip of the C structures rotates with the initial dip of the foliation and forms an angle close to 45° to the Sn. The models with layers stretched during the shear ($\delta_0 > 0$) are marked by the formation of boudins at small obliquity (Type I, Fig. 4a) and shear bands at large obliquity (Type II, Fig. 5a). The models with layers that shorten during shearing ($\delta_0 < 0$), all accommodate the shortening by folding, but, in the models presented here, the finite wavelength of the folds vary with the initial dip of the layers. For initial dips ranging from $\delta_0 = -10^\circ$ to $\delta_0 = -30^\circ$ the foliation is folded at small scale compared to the size of models. The asymmetry of the fold limbs increases as the obliquity of the initial layering increases (Type III, Fig. 6a). At $\delta_0 = -30^\circ$, the asymmetry and the anisotropy are such that kink folds develop (Type IIb). On the opposite, the models with $\delta_0 < -30^\circ$ have their foliation partially or completely ($\delta_0 = -45^\circ$) transposed toward positive values of δ_0. In these cases, C structures begin to develop in the transposed part of the model (Type IV, Fig.7a) at large γ^{bulk}. Only the models with low negative obliquity ($\delta_0 = -10^\circ$ or -20°, i.e. Type IIa) display hardening in the early deformation stages. The models with Sn dipping in the shear direction, i.e. to the right, tend to show no or little softening.

There are large pressure gradients between the weak and strong layers of all of the models. In the types I and II, the pressure is always higher than lithostatic in the weak layers. In the type III case, it is the opposite. The type IV case shows a reversal in the early deformation stages and thereafter mimics the type II case, once some parts of the model are transposed. Only type IV shows a pressure gradient switch during the

SED
4, 1165–1204, 2012

early deformation stages. During this transient event, the deviatoric stresses are about 100 MPa although the pressure gradient is zero. For the initial and final conditions of type IV as well as for all the other cases, the average pressure difference between the weak and the strong phase is approximately equal to the deviatoric stresses in the strong phase, i.e. 100 to 200 MPa.

3 Detailed mechanical insights

3.1 Type I

The finite strain reflects the change in strain partitioning with increasing obliquity of δ_o. This partitioning is outlined both by the large amount of finite shear strain in the weak layers (Fig. 4a) and by the oblique orientation of the MSD versus the current Sn (Fig. 4b). It is particularly visible at $\delta_0 = 10^{\circ}$, where the white lines of the stretching direction are systematically parallel to the layering in the strong layers (pure stretching in the Sn) and oblique to the layering in the weak layers (simple shear flow parallel to the Sn).

Close to the applied shear, the strong layers tend to be cut at high angles by small left dipping shear bands which form a regular geometric pattern of strain in all the models. At small scale, all the Type I cases correspond to boudinage of the strong layers. However, as the obliquity increases, the asymmetry of the boudins increases and the MSD tends to become parallel to the bulk direction of shear in the high strain zones (Fig. 4b, up) rather than being aligned to the Sn (Fig. 4b, down). At high obliquity, the high strain zones tend to coalesce to form incipient top to the left shear bands that dip to the left (hence opposite to the dip of the initial foliation). At low obliquity, we interpret the alignement of the MSD with the Sn as the formation of symmetric boundins within simple shear boundary conditions.

The increasing obliquity also correlates with an increasing depth of penetration of the deformation of the strong layers. Fig. 4a shows that the strong layers tend towards the

SED
4, 1165–1204, 2012

green colour even in the center of the model at $\delta_0 = 30^\circ$, while at $\delta_0 = 10^\circ$ only the top 10 % to 20 % of the model undergoes noticeable deformation in the strong layers. The depth of penetration of the deformation is also correlated with the rise of the average shear stress in the strong layers as obliquity increases (Fig. 4c). All the models that fall into the Type I class show very little softening with bulk strain. This class is also characterised by a constant pressure gap of 100 MPa with a gradient directed from the weak towards the strong layers.

The left lateral displacement is distributed at all depths from the early stage of the bulk deformation (curves on Figs. 4a and 4d for $\gamma^{bulk} = 30\,\%$). The rate of displacement with depth is constant with increasing bulk strain. However, the initial rate of displacement may either be constant with depth (case $\delta_0 = 10^\circ$) resulting in a linear finite displacement profile at $\gamma^{bulk} = 100\,\%$ or more concentrated at the top of the column (case $\delta_0 = 30^\circ$) resulting in a non linear finite displacement profile. Therefore, there is no true localisation of strain with time, i.e. no abandoned shear zones. This steady state behaviour is consistent with the absence of strain weakening demonstrated by the constant deviatoric stress measured in the strong layers.

3.2 Type II

Type II (Fig. 5) differs from Type I by the clear predominance of shear bands over simple shear in the plane of the Sn. Fig. 3 illustrates that the dip of the shear bands depends on the Sn orientation, with left dipping shear bands for $\delta_0 = 40^\circ$, horizontal shear bands for $\delta_0 = 45^\circ$ and slightly right dipping shear bands for $\delta_0 = 50^\circ$. Within the shear bands, the MSD tends to flatten with the intensity of shear strain and to become parallel with the large scale kinematics applied on the boundary of the models (Fig. 5b).

At $\gamma^{bulk} = 100\,\%$, the penetration of the strain with depth is relatively similar in all the models but the number of shear bands and their spacing change with the dip of the shear bands. Looking in more detail at the depth-displacement profiles with increasing bulk strain, one sees that in the $\delta_0 = 40^\circ$ case the rate of displacement with depth does

SED
4, 1165–1204, 2012

not significantly change with increasing bulk strain although the lateral displacement is more concentrated at the top of the profile. In the $\delta_0 = 50^\circ$ case, the shear bands also appear early in the strain history. In that case, the rate of left lateral displacement decreases with increasing bulk strain in the lowest part of the model indicating that strain localisation is occuring from 60 % bulk strain on. In the $\delta_0 = 45^\circ$ case, the localisation of the shear bands seems to occur between 20 % and 40 % of bulk strain when oscillations begin to appear on the left lateral displacement profile. As the amplitude of those oscillations increases, the rate of displacement at depth decreases denoting again that strain localisation occurs at the scale of the model. As for Type I, shear bands form early in the strain history (Fig. 5d). However, the activity of the shear bands located at depth decreases with time for the models with initial layering obliquity of 45° and more.

The progressive strain localisation highlighted in the displacement profiles is compatible with the slight strain weakening with increasing bulk strain observed in the evolution of the deviatoric stress (Fig. 5c). This weakening is maximum for $\delta_0 = 45^\circ$ and corresponds to the drop of average pressure in the weak layers with time. On average, the pressure is equal to the lithostatic pressure but there is a difference of 150 MPa to 100 MPa between the weak and strong layers. The pressure gradient is directed from the weak to the strong layers, as in Type I. The pressure difference between the strong and weak layers is very close to the average deviatoric stress invariant in the strong layers.

3.3 Type III

The Type III models are characterised by small scale folding and a higher pressure in the strong layers than in the weak layers (Figs. 3,6). Thereby this class defines models which are exactly opposite to the Type I pattern. Type III is separated in two sub-types because small obliquity models (Type IIIA) are characterised by strain hardening, while $\delta_0 = -30^\circ$ is characterised by slight strain weakening (Type IIIB, Fig. 6c). After 100 % bulk shear, the amplitude of the folds is higher at high obliquity than at small obliquity (Fig. 3), indicating that the growth rate of the folds rises with increasing obliquity.

SED
4, 1165–1204, 2012

Similarly, the strong layers are still in the deep blue (low strain) at the center of the model for $\delta_0 = -10^\circ$ while for $\delta_0 = -30^\circ$ the entire medium deforms with kinks folds. As the initial obliquity of the layers increases, the penetration depth of folding instability increases (Fig. 6a) and the deviatoric stresses in the strong layers increases (Fig. 6c).

In all the cases, the MSD is roughtly normal to the strong layers (Fig. 6b). Therefore, the shortening of the strong layers is composed of both a folding component and a pure thickening component. For the Type IIIA the MSD is oblique to the weak layers indicating that those layers deform in simple shear. However, for the Type IIIB the MSD is parallel to the layers that dip toward the right within the kink bands and oblique to the weak layers that slightly dip towards the left between the kink bands. The pure stretching domains therefore correspond to upright limbs of the kink folds (Fig. 6b).

The depth-displacement profiles indicate that the deformation is distributed at all depths from the early phase of the deformation. Those profiles have a tendency to linearise with increasing bulk strain (especialy $\delta_0 = -20^\circ$) which would imply that the shear rate increases downward with increasing bulk deformation to become perfectly distributed though the whole medium. This indicates that a natural shear zone forming in such a configuration would widen with increasing strain.

In these models, the pressure is very close to lithostatic in the weak layers and 100 to 150 MPa higher in the strong layers. As noticed earlier for the Types I and II, the strain weakening/hardening is directly related to the drop/rise of the pressure gradients. In the $\delta_0 = -30^\circ$ case, the pressure drops at the onset of the high angle, right dipping, kink bands i.e. at $\gamma^{\text{bulk}} = 50\,\%$. In the hardening cases, the pressure tends to increase with increasing strain in the strong layers (Fig. 6c). In the Type IIIb case, the softening does not correspond to strain localisation at bulk scale but to the rotation of the soft layers towards directions that are more compatible with the bulk strain direction.

SED
4, 1165–1204, 2012

3.4 Type IV

Type IV is characterised by large wavelength folding which rapidly deflects the initial layering (Fig. 3). In the three cases presented, at $\gamma^{bulk} = 100\,\%$, the shear banding is only incipient for the $\delta_0 = -40^\circ$ and $\delta_0 = -50^\circ$. For the case at $\delta_0 = -45^\circ$, shear banding occurs along a horizontal direction only after $\gamma^{bulk} = 130\,\%$ (not shown). The incipient shear bands (dashed lines on Fig. 7a) dip to the right in the $\delta_0 = -40^\circ$ model and slightly to the left in the $\delta_0 = -50^\circ$ case. The dipping direction of the shear bands obtained is opposite to those obtained for the same obliquity in the Type II but the absolute value of their dip are roughly similar.

$\delta_0 = -45^\circ$ marks a transition in the small scale mode of deformation of the strong layers that is best seen in the grey scale part of Fig. 3 (red circle). In the $\delta_0 = -50^\circ$ case the strong layers form mullions with periodic thickening of the black (weak) layers, whereas for $\delta_0 = -40^\circ$ the small scale deformation corresponds to asymmetric folding with a very short reverse limb. This change of small scale deformation is also outlined by the MSD in the weak layers which is almost normal to the layers in the $\delta_0 = -50^\circ$ case and oblique to the layers in the $\delta_0 = -40^\circ$ case in the deepest part of the detailed cross section (Fig. 7b). At $\delta_0 = -45^\circ$, the strong layers do not deform internally. This lack of micro-structures at $\delta_0 = -45^\circ$ forbids the initial structural softening (Schmalholz et al., 2005) that affects the strong layers in the two other cases. As a result, the strong layer are effectively stronger and rotate passively in a simple shear regime as outlined by the obliquity of the MSD to the strong layers. In the weak layers, the shearing is so intense that the MSD is parallel to the current Sn (Fig. 7b).

The pressure gradient between the strong and weak layers switches from directed towards the weak layers, to directed towards the strong layers as the transposition of the layers occurs on Fig. 7c. This switch is synchronous with strain weakening and as the pressure begins to rise in the weak phase, a slight strain hardening occurs in the models. The strain weakening is linear for the $\delta_0 = -40^\circ$ case and very abrupt for the two other cases. The shear bands form late in the history of the deformation.

SED
4, 1165–1204, 2012

They appear as the layers get transposed and are marked by an increase of the lateral displacement at the surface of the depth deformation profiles. It results that, in these cases, the shear localisation propagates downward as the layers get transposed. In the $\delta_0 = -40^\circ$ the depth deformation profile is separated into two areas of constant displacement gradient, i.e. two linear profiles crossing at the base of the transposed domain. In the $\delta_0 = -50^\circ$ case the gradient of displacement decreases more smoothly with depth as marked by the curvy shape of the depth displacement profile. Note, however, that the shear bands formed in the later deformation stages are not as continuous as the shear band that formed in the type II case. They localise at the tip of the mullions and folds and then coalesce progressively.

4 Scalability of the results for $\delta_0 = 40$

In the models presented here, the viscosity contrast was set to 100. It is beyond the scope of the paper to perform a full parametric study of the scaling of the results for all the orientations. Nevertheless, we have concentrated our effort on the $\delta_0 = 40^\circ$ model, which best displays the formation of shear bands associated to extensional crenulation cleavages (ECC). Since we use a linear viscous rheology in the experiments, we can define an average maximum viscous shear stress as

$$\bar{\tau}^{\max} = \mu\, \dot{\gamma}. \quad (1)$$

In our reference set up, the background strain rate is $\dot{\gamma} = 3\,10^{-13}\,\mathrm{s}^{-1}$ and the viscosities of the weak and strong layers are respectively 10^{19} and $10^{21}\,\mathrm{Pa\,s}^{-1}$ reaching average maximum viscous shear stress of 3 MPa and 300 MPa. Because we also use a pressure sensitive plastic yield criteria, it is worth comparing these values with the 300 MPa confining pressure applied to the models. In the reference case, it is clear that the strong layers are close to plastic yielding and the weak layer are very far from reaching the yield criteria.

SED
4, 1165–1204, 2012

Firstly, to test whether the results were independent of the length scale, we have run an experiment in which the dimensions were divided by a factor 100 yielding a total model dimension of 10 by 40 m and initial layer thickness of 30 cm (Fig. 8a). We have kept the viscosities and background strain rate similar as in the reference experiment (Fig. 8f). The results obtained are similar enough to conclude that our models are valid at least from the kilometers scale to the outcrop scales.

The series of experiments framed in the red box on Fig. 8(d, e, f, g) aims at characterising the impact of the strong layer viscosity on the outcome of the models. For larger viscosities, the orientation and the spacing of the shear bands do not change. There is one more shear band in the experiments d and e than in the reference model, and the displacement profiles shows that at the scale of the experiment, the strain is much more localised for viscosity contrast greater or equal to 1000. In the experiment in which the strong layer viscosity is decreased by a factor 10 (Fig. 8g), the displacement profile indicates that strain localisation is weak at the scale of the experiment and the finite strain does not feature proper shear bands. The viscosity of the strong layer is therefore a decisive factor for shear banding to occur at small scale and strain localisation to occur at large scale. The large similarity of the experiments d and e indicates that the localisation process saturates at high viscosity.

The series of experiments framed in the blue box on Fig. 8(b, f, i) aims at verifying the effect of the background strain rate on strain localisation. At lower strain rate, shear banding does not occur nor strain localisation. At higher strain rate, the shear bands are distributed through the entire medium, and their spacing decreases roughly down to the thickness of the Sn. Eventhough the strain is localised at small scale, it is distributed at the scale of the model. For these higher strain rates (Fig. 8i),the shear stress in the weak layers is on the order of 30 MPa and is therefore no longer negligible compared to the plastic yield strength of the strong layers. As a results, the effective viscosity contrast between the layers drops and much less strain occurs in the weak layers probably causing the lack of localisation at large scale.

SED
4, 1165–1204, 2012

The experiment of Fig. 8h was produced by increasing the viscosity of both the weak and strong layers by a factor of 100, and decreasing the background strain rate by a factor of 100 compared to the experiment i. The results obtained are very similar and lead to the conclusion that our results are applicable to a wide range of viscosities and strain rates as long as the viscous stress in the strong layer exceeds the plastic yield strength.

Amongst all the models presented in Fig. 8, only the models b and g do not produce shear bands. Both cases correspond to lowest bound of the maximum viscous shear stress of the strong layer, i.e. 30 MPa, hence one order of magnitude lower than the confining pressure. On the other hand, when the maximum viscous shear stress of the strong layer largely exceeds the yielding criteria, the results are not modified (e.g. experiments d and e). We therefore postulate that although plastic strain is not predominant in the reference model, it is necessary to include a constant yield strength in the rheology of the rock in order to form the localised ECC. In order to confirm this hypothesis, we have run a simulation which is identical to the reference experiment except that plastic yielding was disabled. The results (Fig. 8c) lack the formation of shear bands as did the b and g experiments.

In all the models, one observes the same alignement of large strain structures with a dip of approximately 10–15° towards the left, which indicates that the dip of the C structure is controled by the anisotropy at the beginning of the deformation rather than by the scale, the strain rate or the viscosity contrast. At constant strain rate, our models are lengthscale independent. At large strain rate, shear bands are favored but the strain is more distributed in the model. As the strain becomes more penetrative the flow pattern becomes more linear at large scale. In all the cases, true plastic deformation is a necessary condition for the localisation of shear bands.

These observations suggest that the knowledge of the yield strength of the strong layers is a prerequisite to infer the viscous property of the rocks from field observations. In the model presented here, we have used Mohr Coulomb yield criteria. This choice can be discussed since it is pressure dependent while localised shear bands form

SED
4, 1165–1204, 2012

through the entire lithosphere in nature. This problem can be ruled out if we assess that the low permeability of the lower crust and upper mantle favours undrained conditions and that non-hydrostatic fluid pressure can limit the depth dependence of frictional yield criterion (Sibson, 1994). We also acknowledge that non-newtonian stress dependent rheology could allow the deformation to localise. Dislocation creep would enhanced the growth rate of the small scale shear instabilities but in order to localise shear bands at great depth, a mechanism with a fixed yield strength like Peierls creep (Goetze and Evans, 1979) would probably be better a candidate.

5 Discussion

5.1 Direction of anisotropy and type of structures formed

The paper considers a foliated media where the strength of the weaker layers is two orders of magnitude less than the strength of the stronger layers. Assuming that stresses are continuous across the interface between the strong and the weak layers, one finds that the shear stress and the normal stress acting on the interface of the layers, i.e. the local Sn plane, must be the same in both layers. The shear strength of the weak layers being negligible, it may be considered as a good approximation to say that the shear stress along the Sn is close to zero. This implies by definition that, at the smaller scale, the Sn is one of the principal stress axis within the strong layers. Therefore, at small scale the hypothesis of Biot (1964) is always satisfied. A second implication of the continuity of stress is that the deviatoric stress in the strong layer must be equal to the gap of pressure between the strong and weak layer. Implication that is confirmed by the monitoring of the stress and pressure presented in Figs. 4c, 5c, 6c and 7c. It results that the sign of the pressure difference defines if the orientation of the Sn (reported with a square on Fig. 9) supports σ_1 or σ_3.

Accounting for this local orientation of the principal stress axis, we may draw the maximum shear stress axes within the strong layers (a and b on Fig. 9) and define

SED
4, 1165–1204, 2012

the kinematics of the corresponding shear zones according to the local principal stress orientation. After reporting the a and b axis on the representation of shear strain at $\gamma^{bulk} = 10\,\%$, and comparing with the preferred shear orientations at $\gamma = 100\,\%$ on Fig. 3, we show that for the types I, II and IV, the orientation of the newly formed shear bands is acquired at the early beginning of the deformation. The fact that the shear localisation directions are acquired at very small strain indeed explains *a posteriori* why the small strain formulation of Biot (1964) allows retrieving the orientation of large strain feature like kink bands and ECC (Cosgrove, 1976).

At the macro scale, the C structures correspond only to one of the two conjugate local maximum shear orientations, i.e. the one compatible with the larger scale flow direction. In the Type I, the chosen orientation is relatively similar to the extensional crenulation cleavage first described by Platt and Vissers (1980) or to the C' orientation in primarily isotropic medium (Berthé et al., 1979). In the Type II and IV case, the chosen orientation correspond to one of a neoformed shear band and forms S-C structures together with the Sn. Finally, in the Type III case the orientation b corresponds to a true crenulation cleavage. In conclusion, all types of micro-structures can form within the same boundary conditions. While the boundary conditions control the overall kinematics, the direction of the initial anisotropy controls the type of micro-structures that form and the effective strength of the sheared media. Considering the relation between meso-scale and microscale structure, it is obvious that as structure rotates at the mesoscale, the rocks may go through cycle of hardening (folding) and weakening (thining) at the microscale and give rise to anastomosed shearzone as was already pointed out by Ghosh and Sengupta (1987).

5.2 Petrological implications of the pressure gradients

The weak and strong layers of the models sustain very different pressure values which deviate by one fourth to one half of the confining pressure applied at the boundary. We have found that the amplitude depends on the effective strength of the strong layers and that the sense of the gradient depends on its orientation versus the shear direction. The

SED
4, 1165–1204, 2012

pressure gap we computed are half of the amplitude found for very elongated ellipse clasts and the relationship with the orientation shows similar trends as Schmid (2005) found around rigid inclusions.

These so called tectonic over/under pressures are rarely reported in the rocks (with exception of (Vrijmoed et al., 2009)) but predicted by all the models in use in geodynamics (see Mancktelow (2008) for review). Our models predict that for $\gamma^{bulk} > 120\,\%$ the pressure is very close to lithostatic in the weak deforming part of the model, regardless of initial orientation. Accounting that dynamic recrystallisations and therefore synkinematic paragenesis are more likely to occur in the weakest part of the rock, our model could provide an explanation for the scarcity of proven examples of tectonic over/under pressure in rocks. Incidently, the pressure difference we predict is on the order of the strength of the stronger layers of the rocks, i.e. close to 100 MPa, which compares with the error bar of thermobarometric methods.

On the other hand, large pressure differences at small scales induce large pressure gradients, which, according to our model, are maintained as long as deformation continues. Pressure gradients contribute to chemical potential differences and mineral solubilities without increasing the permeability of the crust. For example, this mechanism induces the dissolution of a mineral like quartz in high-pressure domains and its precipitation in low-pressure domains (Fletcher, 1977). We postulate that, in anisotropic media, veins could form by diffusive small-scale mass transfer enhanced by large and long-lived local pressure gradients rather than by large-scale advective mass transfer which requires seemingly unrealistic quantities of external water (Ferry and Dipple, 1991). Following this hypothesis, our model would thus predict that elements migrate toward the strong layers in Types I and II regime and that quartz veins may form in the weaker layers in type III and in the early deformation stages for Type IV orientations. More work is needed in order to quantify the scale at which this process may become effective.

SED
4, 1165–1204, 2012

5.3 Reconstructing the strain history

This theoretical study has implications on the interpretation of deformation in anisotropic rocks observed in the field. We have shown that for a given simple shear kinematics, all kind of micro-stuctures can form as a function of the initial orientation of the pre-existing foliation or stratification relative to shear strain field. In all cases, the kinematics indicated by the shear-bands or the asymmetry of folds has been shown to be consistent with the sense of shear at the boundary, whatever the initial direction of the layers. We note however that due to the anisotropy of the media, the neoformed shear bands are rarely parallel to the direction of the shear (except for $\delta_0 = \pm 45^\circ$). As a result, although simple shear was applied at the boundary, the shear bands dipping towards the sense of shear display a normal kinematics and those with an opposite dipping sense display a reverse kinematics. Similarly, we have shown that the observation of a lineation parallel to the Sn between boudins does not proove that the larger scale deformation is in pure shear mode (see the $\delta_0 = 20^\circ$ case).

The models presented here show that the sense of shear on the neoformed shear bands is always compatible with the large scale sense of shear. As the orientation of the shear bands is acquired very early in the deformation history, the geometry of the shear bands provides information on the inital orientation of the layering. We provide below such examples of natural S-C structures where the intial orientation can be constrained. Fig. 10a and b displays examples from the Betics in Spain which scaling, orientations and localisation are described in detail by Agard et al. (2011). According to our models, the lack of rotation of the S between the C indicates that the original foliation was dipping in the opposite direction to the sense of shear. 10a strictly resembles type II while the slight variation of dip and the length scale of the shear band on picture b would fall in between type I and II suggesting that the initial schistosity was dipping with slightly smaller angle. 10c and d are examples from the Tende shear zone in Corsica, France. In both cases, the foliation is folded between the shear zone indicating that the initial foliation would have been dipping toward the sense

SED
4, 1165–1204, 2012

of shear initially. While Fig. 10d resemble a type III, the Fig. 10c is a clear example of type IV S-C structures.

Our models also show that localised deformation that crosscuts the initial foliation, i.e. shear bands, only occurs for a restricted range of initial orientation of the layering (types II and IV). On the one hand, the models have shown that the occurrence C structures requires that the strong layers yield plastically, implying that

$$\mu^{\text{strong}} > \tau_y/\dot{\gamma}, \tag{2}$$

where μ^{strong}, τ_y and $\dot{\gamma}$ stand respectively for the viscosity of the strong layers, the plastic yield strength and the background strain rate. On the other hand, large scale strain localisation requires that the weak layer does not yield plastically, and hence

$$\mu^{\text{weak}} < \tau_y/\dot{\gamma}, \tag{3}$$

where μ^{weak} is the visosity of the weak layer. Therefore, providing that both the plastic yield strength and the large scale kinematics are known, the microstructure and the observation of strain localisation at larger scale in turn provide bounds on the viscosity of the strong layers. Conversely, one could use the laboratory data on creep parameters and plastic yield strengths to estimate the large scale strain rate.

6 Conclusions

We have run numerical experiments to simulate the deformation of mechanicaly stratified medium in simple shear in order to provide quantitative insights on the microstructures forming in that context as a function of the initial orientation of the layers relative to shear strain field. The results obtained are representative of the diversity of natural microstructures and highlight that the formation of shear bands, extensional crenulation cleavage, symmetric boudinage, micro-folds and kink bands is independent of the geological context but rather depends on the initial orientation of the anisotropy. This

SED
4, 1165–1204, 2012

implies that one must be careful in interpreting the shape of the boudins or folds as indicators for simple shear or pure shear at large scales.

The simulations have been separated into four groups depending on the absolute value of the initial dip, δ_0, and its sign. The absolute value of δ_0 controls strain partitioning between the weak and strong layers and its sign controls the effective shortening or stretching of the layers as they rotate within the shear zone. We herein demonstrate that the initial orientation of the anisotropy controls the dip of the shear bands, the degree of localisation and the microstructures that can form in a large scale shear zone. At local scale, the maximum shear stress orientation in the strong layers that is the closest to the large scale flow is always selected to localise the strain. Therefore, at the regional or model scale, the shear sense on the microstructure is fixed by the plate kinematics or the boundary conditions. However, depending on the orientation of the initial anisotropy, the selected maximum shear direction corresponds alternatively to extensional crenulation cleavage (type I), C structures (type II and IV) and true crenulation (type III).

All the experiments show that anisotropy results in non-lithostatic pressure values which are proportional to the deviatoric stresses in the strong layer. Since this strength is limited by the plastic yield strength of the layer, for a confining pressure of 4 kbar, we never found deviations of more than 1.5 kbar at the onset of the deformation. These deviations are in the error bars of thermobarometric estimations based on thermodynamic methods. However, given the scale independance of the results, we speculate that these large pressure jumps can result in large pressure gradients at small scale and therefore influence the chemical potential of elements in the crust and their rate of migration.

We have also shown that our results are scale independant and that the orientation of the shear bands is acquired in the early deformation stages and remains independant of the strong layer viscosity or the strain rate. We demonstrate here that viscous rheology alone is not sufficient to model the diversity of microstructures observed in the ductile crust and that introducing some finite yield strength (e.g. brittle processes)

SED
4, 1165–1204, 2012

in the rheological model of the ductile crust allows reproducing this diversity. Finally, we find that the main controlling parameters for the localisation of shear bands at small scale is the ability of the strong layers to yield plastically, but that strain localisation at larger scale only occurs when the orientation of the anisotropy is initialy forming an angle of at least 40° to the shear zone and when the weak layers deform viscously.

Appendix A

Equations solved

We use the numerical code Paravoz (Poliakov et al., 1993b,a) an academic implementation of FLAC algorithm (Cundall and Board, 1988). In this study, we only make use of the part of the code that solves for momentum equilibrium, which reaches

$$\frac{D\sigma_{ij}}{Dx_j} = \rho\ddot{u} \simeq 0, \tag{A1}$$

if one neglects the effect of gravity. The code uses visco-elastic / elasto-plastic rheologies. The elastic part of the rheology is best described by splitting the volumetric compressible component of Hookes law, that relates the pressure P to the elastic volumetric strain ϵ^e_{ii} (Einstein summation applies)

$$\bar{\sigma} = -P = K\epsilon^e_{ii}, \tag{A2}$$

of its incompressible shear component (denoted by $\tilde{}$)

$$\tilde{\sigma}_{ij} = 2\,G\,\tilde{\epsilon}^e_{ij}. \tag{A3}$$

The elastic shear stress is either relaxed by a linear viscous component (denoted by ^{v}) or a plastic component (denoted by ^{p}) depending on the weakest relaxation mechanism so that

$$\dot{\tilde{\sigma}} = \min\left[2\,G\,\left(\dot{\tilde{\epsilon}} - \dot{\tilde{\epsilon}}^v\right),\, 2\,G\,\left(\dot{\tilde{\epsilon}} - \dot{\tilde{\epsilon}}^p\right)\right] \tag{A4}$$

SED
4, 1165–1204, 2012

where $\dot{\tilde{\epsilon}}$ is the deviatoric strain rate. The viscous relaxation corresponds to a viscous strain rate of

$$\dot{\tilde{\epsilon}}^{v}_{ij} = \frac{\tilde{\sigma}_{ij}}{2\mu}, \tag{A5}$$

while incompressible Mohr-Coulomb plastic flow is derived from the plastic potential

$$Q = \frac{\sigma_1 - \sigma_3}{2}, \tag{A6}$$

according to

$$\dot{\tilde{\epsilon}}^{p}_{ij} = \lambda \frac{\partial Q}{\partial \sigma_{ij}}. \tag{A7}$$

The scalar multiplier λ ensures that the yield criterion

$$F = \frac{\sigma_1 - \sigma_3}{2} - \frac{\sigma_1 + \sigma_3}{2} \sin\phi - C_o \cos\phi = 0, \tag{A8}$$

is respected during plastic flow of a material of friction angle ϕ and Cohesion C_o (Vermeer and De Borst, 1984).

Paravoz uses an explicit time marching algorithm which limits the time step to half of the smallest Maxwell relaxation time in the model. Although each increment of strain is small, Jauman corrotational corrections are applied to ensure the objectivity of the stress/strain update at each time step. The code is implemented in a fully Lagrangian formulation. Therefore, large strain simulations require re-meshing to ensure the quality of the mesh is sufficient to obtain an accurate solution at each timestep. However, re-meshing also introduces two kinds of errors during the simulation, stress oscillations and numerical diffusion of phases/material. It is difficult to correct the stress tensor components after re-meshing because they cannot be interpolated. However, the oscillations are easily recognized from the longer term signal in the results. Throughout

SED
4, 1165–1204, 2012

this paper we make no attempt to interpret the oscillations as being associated with any physical process. Numerical diffusion is reduced using the re-meshing algorithm described in Yamato et al. (2007), which is based on the implementation of passive markers. These passive markers are also used to post-process the finite strain using a method described hereafter.

Appendix B

Representation of the results

The results of the models are represented by superimposing the lithology in grey scale with the finite strain in colour scale. The black and grey areas represent respectively the weak and strong layers of the models and define the deformed original foliation Sn. For the more detailed region of the domain (white box in Fig. 1b), we also represent the local maximum stretching direction (MSD) with white lines. Since the models presented here are 2-D plane strain, the MSD is equivalent to the trace of the maximum flattening plane, which corresponds in the rocks to the schistosity or the foliation. As we do not account for mineral transformations, we will interpret the MSD as being the direction of an incipient schistosity. The colour scale denotes the amount of finite strain with blue and red indicating the low strain islands and the large strain domains respectively.

In order to compute the finite strain, we use the passive markers implemented by Yamato et al. (2007) and a geometric method derived from Ramsay and Huber (1983). The method was initialy derived for triangles and has been extended to quadrilaterals for the purpose of this study. For each quadrilateral element of the passive marker mesh, the finite strain is obtained in two steps.

Each quadrilateral mesh is composed of four passive markers which defines four vectors

$$X_i^{\mathrm{ini}} = \left[x_i^{\mathrm{ini}} \; y_i^{\mathrm{ini}} \right]^t, \; i = 1,2,3,4 \qquad \text{(B1)}$$

SED
4, 1165–1204, 2012

in the initial configuration (see Fig. 2). Similarly, in the final configuration the passive markers define four vectors

$$X_i^{\text{fin}} = \left[x_i^{\text{fin}} \; y_i^{\text{fin}} \right]^t, \; i = 1,2,3,4. \tag{B2}$$

The initial and final vectors are related to one an other through the deformation matrices

$$X_i^{\text{fin}} = S_i X_i^{\text{ini}}, \text{ with } S_i = \begin{bmatrix} a_i & b_i \\ c_i & d_i \end{bmatrix}, \; i = 1,2,3,4, \tag{B3}$$

defined in Ramsay and Huber (1983).

At large strain, the final mesh is not always a parallelogram (Fig.2b). Therefore the four matrices S_i differ from each other. For visualisation purposes, an equivalent matrix S must be defined for each quadrilateral element. We compute it using a least square inversion procedure for the four equations defined in eq.B3.

In the second step we compute the parameters of the finite strain from the equivalent strain matrix (Ramsay and Huber, 1983). The orientation of the maximum stretching axis of the finite strain tensor (θ') is infered from

$$\tan(2\theta') = \frac{2(ac+bd)}{a^2+b^2-c^2-d^2}. \tag{B4}$$

This direction is represented with white line on the details snapshot of the models. The intensity of stretching in that direction is

$$L_1 = \frac{1}{2}\sqrt{\frac{a^2+b^2+c^2+d^2+\sqrt{\left(a^2-b^2+c^2-d^2\right)^2+4(ab+cd)^2}}{2}}, \tag{B5}$$

and the intensity of maximum shortening (normal to the direction of θ') is

$$L_2 = \frac{1}{2}\sqrt{\frac{a^2+b^2+c^2+d^2-\sqrt{\left(a^2-b^2+c^2-d^2\right)^2+4(ab+cd)^2}}{2}}. \tag{B6}$$

SED
4, 1165–1204, 2012

The ellipticity

$$R = L_1/L_2 \tag{B7}$$

is a measure of the intensity of the finite strain which varies between 1 (no strain) and $+\infty$ (infinite strain). For visualisation purposes, we prefer to use

$$R' = 1 - 1/R. \tag{B8}$$

which renormalises the finite strain on a hyperbolic scale that varies between 0 (no strain, blue on the figures) and 1 (infinite strain, red on the figures).

Acknowledgements. Project financed by INSU 3F program. The authors thank O. Vidal, A. Verlaguet and J. Saleeby for fruitful discussions.

References

Agard, P., Augier, R., and Monié, P.: Shear band formation vs. progressive deformation on a regional scale: evidence from anisotropic rocks near a major contact (Betic Cordilleras, Spain), J. Struct. Geol., 33, 114–131,2011. 1183

1168

Avallone, A., Briole, P., Agatza-Balodimou, A., Billiris, H., Charade, O., Mitsakaki, C., Nercessian, A., Papazissi, K., Paradissis, D., and Veis, G.: Analysis of eleven years of deformation measured by GPS in the Corinth Rift Laboratory area, Comptes Rendus Geosciences, 336, 301–311, 2004.

Berthé, D., Choukroune, P., and Jegouzo, P.: Orthogneiss, mylonite and non coaxial deformation of granites: the example of the South Armorican Shear Zone, J. Struct. Geol., 1, 31–42, 1979. 1181

Biot, M.: Theory of internal buckling of a confined multilayered structure, Geol. Soc. Am. Bull., 75, 563, 1964. 1167, 1180, 1181

Carreras, J.: Zooming on Northern Cap de Creus shear zones, Journal of Structural Geology, 23, 1457–1486, doi:10.1016/S0191-8141(01)00011-6, http://www.sciencedirect.com/science/article/B6V9D-43DDV09-B/2/a3659976a7640bc21393eb00e5b95f09, 2001. 1167

SED

4, 1165–1204, 2012

Choukroune, P., Gapais, D., and Merle, O.: Shear criteria and structural symmetry, J. Struct. Geol., 9, 525–530, doi:10.1016/0191-8141(87)90137-4, http://www.sciencedirect.com/science/article/B6V9D-488G8KW-2R/2/0661d98f6601b0038bc82bcbcd639045, shear Criteria in Rocks, 1987. 1167

Cloos, E.: Lineation, a critical review and annotated bibliography: Geol, Soc. America Mem, 18, 1948, 1946. 1167

Cobbold, P., Cosgrove, J., and Summers, J.: Development of internal structures in deformed anisotropic rocks, Tectonophysics, 12, 23–53, doi:10.1016/0040-1951(71)90065-5, http://www.sciencedirect.com/science/article/B6V72-48BK86V-10/2/a36d1bb18b1e54025c761834363cb470, 1971. 1167, 1169

Cosgrove, J.: The formation of crenulation cleavage, J. Geol. Soc., 132, 155, 1976. 1167, 1181

Cosgrove, J. W.: The use of shear zones and related structures as kinematic indicators: a review, Geol. Soc., London, Special Publications, 272, 59–74, doi:10.1144/GSL.SP.2007.272.01.05, http://sp.lyellcollection.org/cgi/content/abstract/272/1/59, 2007. 1167

Cundall, P. and Board, M.: A microcomputer program for modeling large-strain plasticity problems, Numerical methods in geomechanics, 6, 2101–2108, 1988. 1186

Ferry, J. and Dipple, G.: Fluid flow, mineral reactions, and metasomatism, Geology, 19, 211, 1991. 1182

Fletcher, R.: Quantitative theory for metamorphic differentiation in development of crenulation cleavage, Geology, 5, 185, 1977. 1182

Frehner, M., Exner, U., Mancktelow, N., and Grujic, D.: The not-so-simple effects of boundary conditions on models of simple shear, Geology, 39, 719–722, 2011. 1167

Fusseis, F., Handy, M., and Schrank, C.: Networking of shear zones at the brittle-to-viscous transition (Cap de Creus, NE Spain), J. Struct. Geol., 28, 1228–1243, doi:10.1016/j.jsg.2006.03.022, http://www.sciencedirect.com/science/article/B6V9D-4JX370W-1/2/9689ac7567c0d348d5a80cd52933d6aa, 2006. 1168

Ghosh, S. and Sengupta, S.: Progressive development of structures in a ductile shear zone, J. Struct. Geol., 9, 277–287, doi:10.1016/0191-8141(87)90052-6, http://www.sciencedirect.com/science/article/B6V9D-48CG802-34/2/c5223dfe8674bfd5dd99f7e4bde79d87, 1987. 1181

SED
4, 1165–1204, 2012

Goetze, C. and Evans, B.: Stress and temperature in the bending lithosphere as constrained by experimental rock mechanics, Geophysical Journal of the Royal Astronomical Society, 59, 463–478, 1979. 1180

Handy, M. R., Babist, J., Wagner, R., Rosenberg, C., and Konrad, M.: Decoupling and its relation to strain partitioning in continental lithosphere: insight from the Periadriatic fault system (European Alps), Geolog. Soc., London, Special Publications, 243, 249–276, doi:10.1144/GSL.SP.2005.243.01.17, http://sp.lyellcollection.org/cgi/content/abstract/243/1/249, 2005. 1168

Hanmer, S. and Passchier, C.: Shear-sense indicators: a review, Geological Survey of Canada Paper, 1991. 1166

Hippertt, J.: Are S-C structures, duplexes and conjugate shear zones different manifestations of the same scale-invariant phenomenon?, Journal of Structural Geology, 21, 975–984, doi:10.1016/S0191-8141(99)00047-4, http://www.sciencedirect.com/science/article/B6V9D-3X2HYRH-D/2/8e417fe2568c30423fa021155db3e862, 1999. 1166

Jolivet, L., Lecomte, E., Huet, B., Denčle, Y., Lacombe, O., Labrousse, L., Le Pourhiet, L., and Mehl, C.: The north cycladic detachment system, Earth Planet. Sci. Lett., 289, 87–104, 2010. 1168

Le Pourhiet, L.: Strain Localization Due to Structural Softening During Pressure Sensitive Rate Independent Yielding, Bulletin de la Societé Géologique de France, special issue in honor of J. Angelier, accepted, 2012. 1168

Leloup, P., Lacassin, R., Tapponnier, P., Schärer, U., Dalai, Z., Xiaohan, L., Liangshang, Z., Shaocheng, J., and Trinh, P.: The Ailao Shan-Red River shear zone (Yunnan, China), Tertiary transform boundary of Indochina, Tectonophysics, 251, 3–10, 1995. 1168

Lister, G. and Williams, P.: The partitioning of deformation in flowing rock masses, Tectonophysics, 92, 1–33, 1983. 1167

Mancktelow, N.: How ductile are ductile shear zones?, Geology, 34, 345, 2006. 1167, 1168

Mancktelow, N. S.: Tectonic pressure: Theoretical concepts and modelled examples, Lithos, 103, 149–177, doi:10.1016/j.lithos.2007.09.013, http://www.sciencedirect.com/science/article/B6V6J-4PTDV99-6/2/a61d816be93461f4db59b904b827232b, rocks Generated under Extreme Pressure and Temperature Conditions: Mechanisms, Concepts, Models, 2008. 1182

Michibayashi, K. and Murakami, M.: Development of a shear band cleavage as a result of strain partitioning, J. Struct. Geol., 29, 1070–1082, 2007. 1167

SED
4, 1165–1204, 2012

Muhlhaus, H., Moresi, L., Hobbs, B., and Dufour, F.: Large amplitude folding in finely layered viscoelastic rock structures, Pure Appl. Geophys., 159, 2311–2333, 2002. 1167
Muhlhaus, H., Moresi, L., and Cada, M.: Emergent anisotropy and flow alignment in viscous rock, Pure Appl. Geophys., 161, 2451–2463, 2004. 1167
Platt, J.: Secondary cleavages in ductile shear zones, J. Struct. Geol., 6, 439–442, doi:10.1016/0191-8141(84)90045-2, http://www.sciencedirect.com/science/article/B6V9D-4887Y24-5D/2/1560cf3914c92e47b77b11cf0d53218b, 1984. 1167
Platt, J. and Vissers, R.: Extensional structures in anisotropic rocks, J. Struct. Geol., 2, 397–410, doi:10.1016/0191-8141(80)90002-4, http://www.sciencedirect.com/science/article/B6V9D-4887XWK-33/2/39a0ce55ab8a530229242847a7f5523c, 1980. 1167, 1168, 1181
Poliakov, A., Cundall, P., Podladchkov, Y., and Lyakhovsky, V.: An explicit inertial method for the simulation of viscoelastic flow: an evaluation of elastic effects on diapiric flow in two- and three-layers models, Flow and Creep in the Solar System: observations, modeling and Theory, 175–195, 1993a. 1186
Poliakov, A., Podladchikov, Y., and Talbot, C.: Initiation of salt diapirs with frictional overburdens: numerical experiments, Tectonophysics, 228, 199–210, 1993b. 1186
Ramsay, J.: Shear zone geometry: A review, J. Struct. Geol., 2, 83–99, doi:10.1016/0191-8141(80)90038-3, http://www.sciencedirect.com/science/article/B6V9D-487DKJD-F/2/03769611226c779767f1a57297f84e57, shear zones in rocks, 1980. 1167
Ramsay, J. and Huber, M.: The Techniques of Modern Structural Geology Volume 1: Strain Analysis, Academic Press, London, 1983. 1188, 1189
Schmalholz, S., Podladchikov, Y., and Jamtveit, B.: Structural softening of the lithosphere, Terra Nova, 17, 66–72, 2005. 1176
Schmid, D.: Rigid polygons in shear, High-strain zones: structure and physical properties, 421, 2005. 1182
Sibson, R. H.: Crustal stress, faulting and fluid flow, Geol. Soc., London, Special Publications, 78, 69–84, doi:10.1144/GSL.SP.1994.078.01.07, http://sp.lyellcollection.org/cgi/content/abstract/78/1/69, 1994. 1180
Simpson, C. and Schmid, S. M.: An evaluation of criteria to deduce the sense of movement in sheared rocks, Geol. Soc. Am. Bull., 94, 1281–1288, doi:10.1130/0016-7606(1983)94¡1281:AEOCTD¿2.0.CO;2, http://gsabulletin.gsapubs.org/content/94/11/1281.abstract, 1983. 1166

SED
4, 1165–1204, 2012

Vermeer, P. and De Borst, R.: Non-associated plasticity for soils, concrete and rock, Heron, 29, 1–64, 1984. 1168, 1187

Vrijmoed, J., Podladchikov, Y., Andersen, T., and Hartz, E.: An alternative model for ultra-high pressure in the Svartberget Fe-Ti garnet-peridotite, Western Gneiss Region, Norway, Europ. J. Mineral., 21, 1119, 2009. 1182

Yamato, P., Agard, P., Burov, E., Le Pourhiet, L., Jolivet, L., and Tiberi, C.: Burial and exhumation in a subduction wedge: Mutual constraints from thermomechanical modeling and natural PTt data (Schistes Lustrés, western Alps), J. Geophys. Res, 112, 2007.

1188

SED

4, 1165–1204, 2012

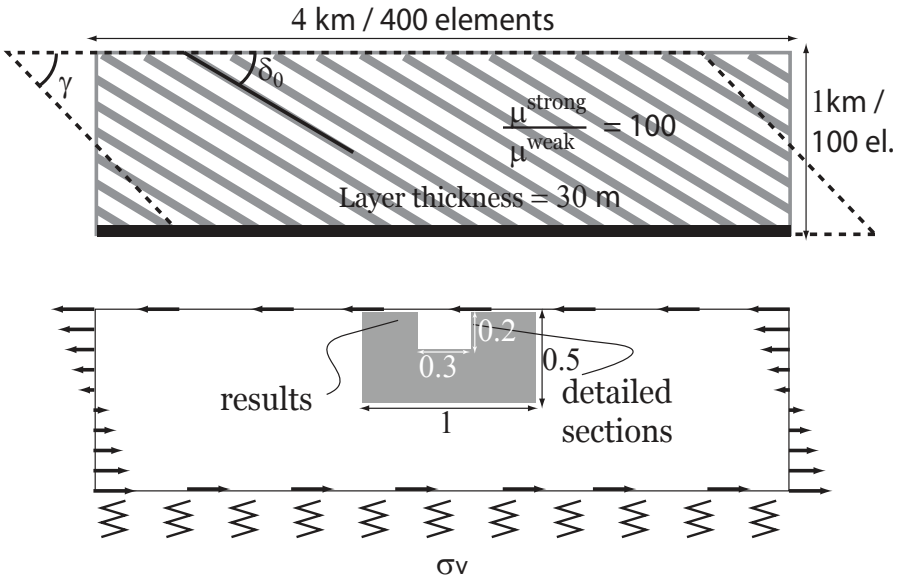

Fig. 1. Modelling set up, initial geometry and boundary conditions.

SED
4, 1165–1204, 2012

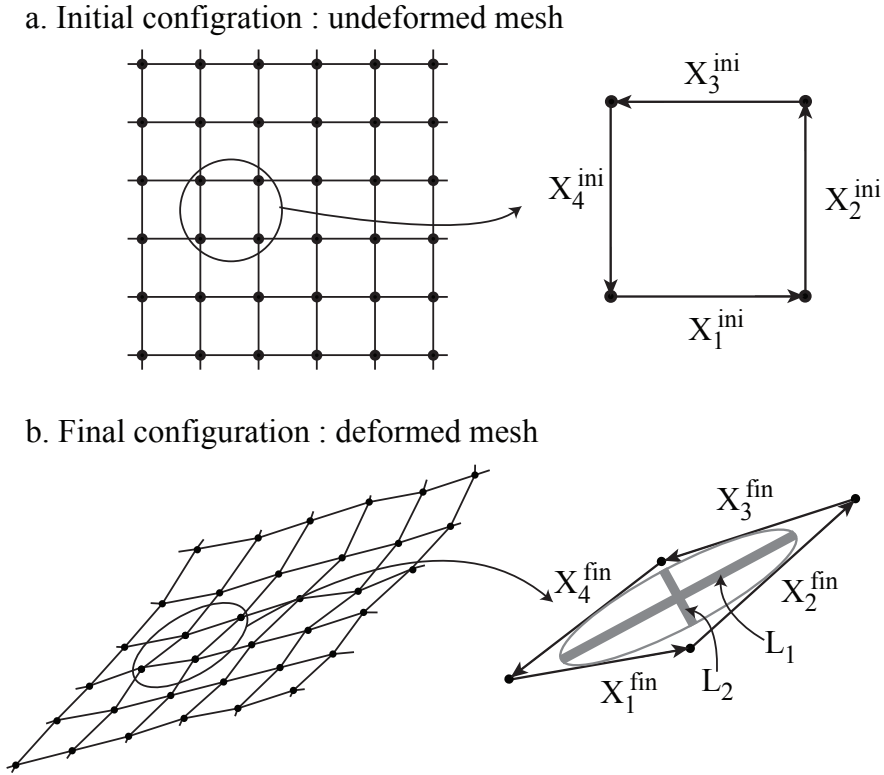

Fig. 2. Schematic representation of the passive marker mesh in the initial configuration **(a)** and final configuration **(b)**. The vectors X_i^{ini} and X_i^{fin} characterise the mesh and allow computing the finite strain.

SED
4, 1165–1204, 2012

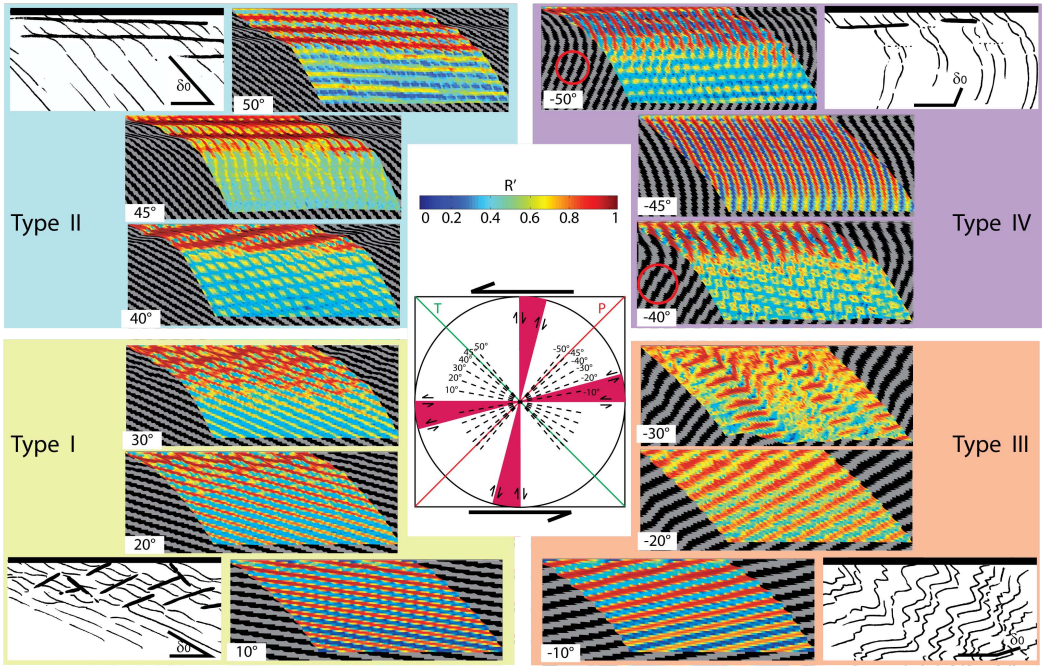

Fig. 3. Results of the parametric study at γ^{bulk} =100 %, accompanied by sketches of the results. Black and grey indicate respectively the location of the weak and strong layers (Sn), the color scale indicates the intensity of strain. The red circles refer to specific small scale folds and mullions described in the text. P and T are respectively the instantaneous shortening and stretching axis at large scale. Maximum large scale shear directions are indicated in magenta.

SED
4, 1165–1204, 2012

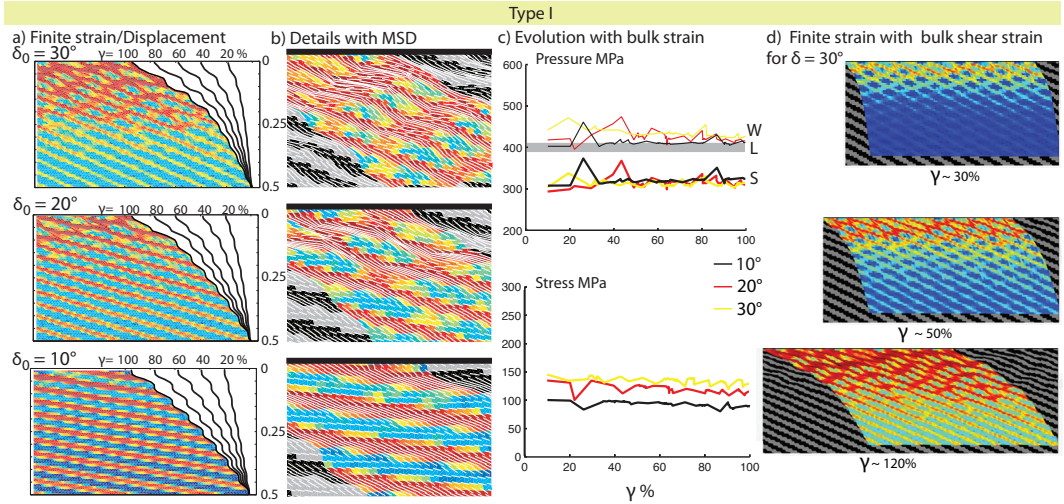

Fig. 4. Type I **(a)** The colour scale indicates the intensity of strain. Most of the strain concentrates in the weak layers with an increasing strain in the strong layers as obliquity increases. The displacement profiles (solid black lines) indicate no clear localisation of the deformation with bulk strain. **(b)** The MSD (white lines) indicates stretching of the strong layers and simple shearing of the weak layers. **(c)** Evolution of pressure and deviatoric stress for the weak (W, thin lines) and strong (S,thick lines) suggest the stationarity of stress and a pressure gap between the strong and weak layers. Applied lithostatic pressure (L) is outlined by a thick grey line **(d)** The evolution of finite strain with time for the $\delta_0 = 30^\circ$ model suggests that the distribution of strain rate with depth is aquired in the early stage.

SED
4, 1165–1204, 2012

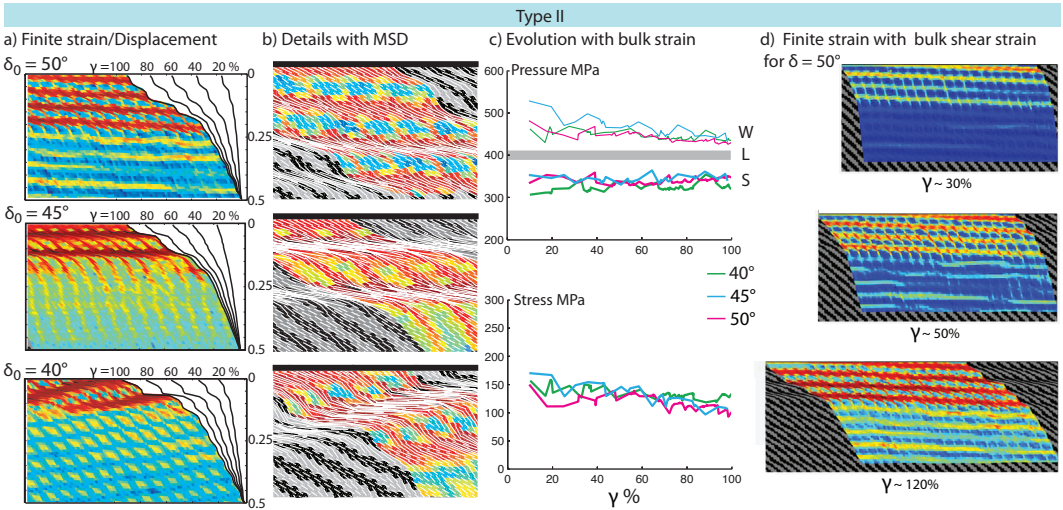

Fig. 5. Type II **(a)** The intensity of strain (colour scale) is maximum on shear bands rather than on the weak layers of the Sn. The deformed profile for γ^{bulk} respectively equal to 20, 40, 60, 80 and 100 % indicate that the rate of displacement decreases with time at depth. **(b)** In the shear bands, the MSD tends to be parallel to the bulk shear at large strain. **(c)** The pressure gap between the weak (W, thin lines) and strong (S, thick lines) as well as the deviatoric stresses decrease with time indicating strain softening. **(d)** The evolution of finite strain with time for $\delta_0 = 50^\circ$ indicates that the deeper shear bands are active from the onset of the deformation.

SED
4, 1165–1204, 2012

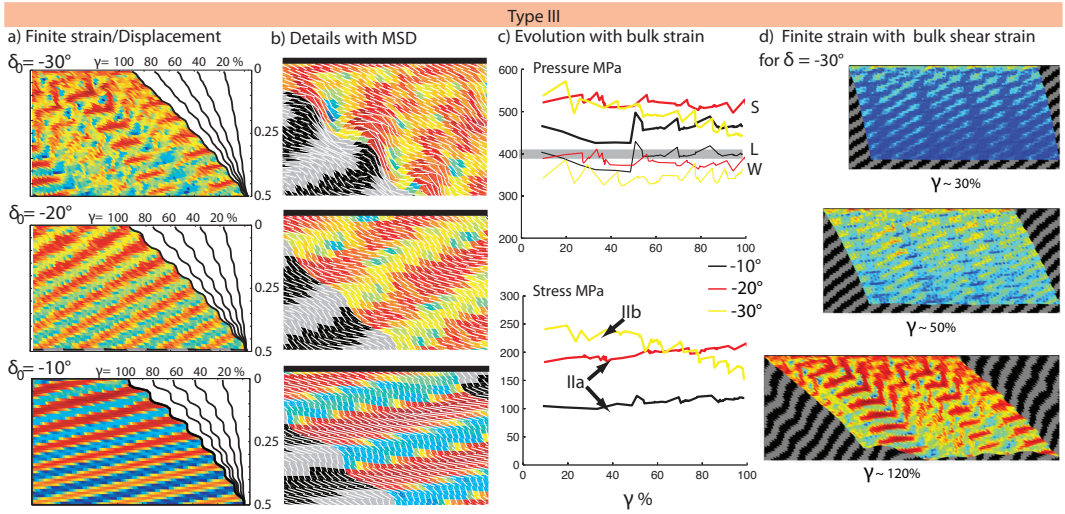

Fig. 6. Type III **(a)** The intensity of strain (colour scale) is maximum in the weak layers and distributed on small scale folds at all depths. The deformed profile for γ^{bulk} respectively equal to 20, 40, 60, 80 and 100 % indicate no localisation with time as displacement rate are roughly constant with increasing bulk strain. **(b)** The MSD (white lines) indicates pure thickening of the strong layers. **(c)** The pressure in the weak layer (W, thin line) is very close to the lithostatic pressure (L) while the pressure in the strong layer (S, thick line) is above lithostatic. The evolution of deviatoric stress discriminates between type IIa and IIb. **(d)** The $\delta_0 = 30^\circ$ model is affected by kink bands that develop with the onset of strain softening.

SED
4, 1165–1204, 2012

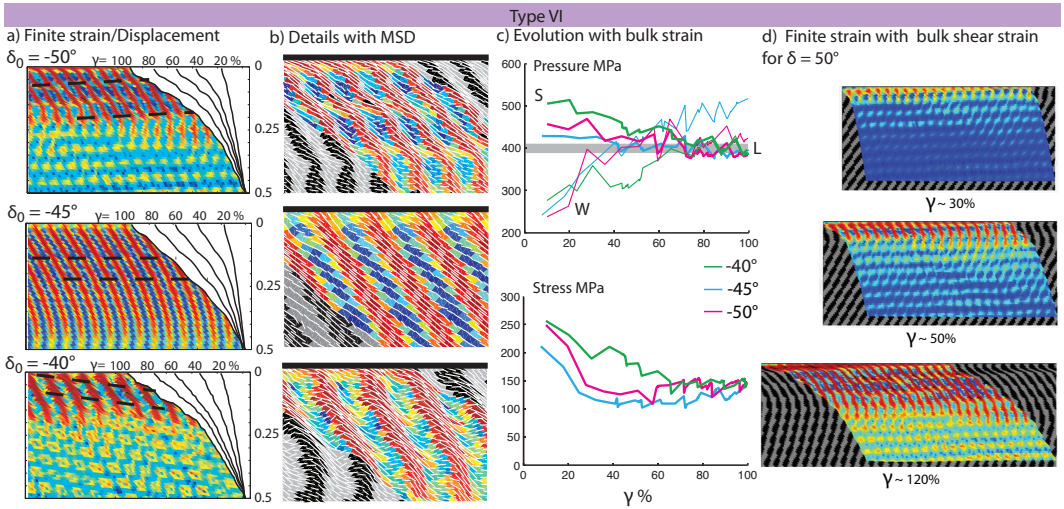

Fig. 7. Type IV **(a)** The maximum shear strain in red is located in the weak layers and incipient shear bands orientations are outlined by dashed line. The depth deformation profiles for γ^{bulk} respectively equal to 20, 40, 60, 80 and 100 % show a progressive migration of the deformation towards depth and no localisation in the $\delta_0 = -45^\circ$ case. **(b)** The MSD indicates that "banc sur banc" predominates. **(c)** The pressure gradient between the strong (S) and weak (W) layers switches with bulk strain at values close to lithostatic pressure (L) and correponds to a dramatic drop of the deviatoric stress in the weak strong layers. **(d)** for $\delta_0 = -50^\circ$, the localisation of shear bands propagates downwards as the layers get transposed and the initial mullions turn into sheared asymetric boundins.

SED
4, 1165–1204, 2012

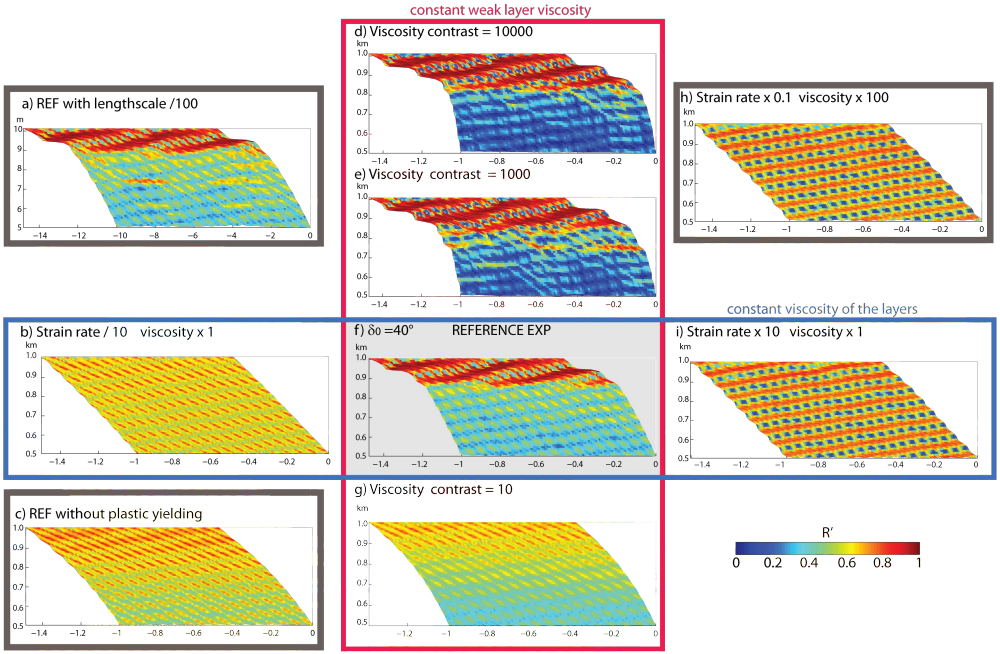

Fig. 8. The blue box represents the effect of varying the back ground strain rate. The red box displays the influence of the strength of the strong layers. The reference model presented on panel **(f)** is the modeled labeled $\delta_0 = 40^{\circ}$ in the text. The grey frames denote three special runs. Panel **(a)** is a run with a 10 by 40 m scale, panel **(c)** is a run without plastic yielding and panel **(h)** is a run with similar viscous shear stress as in panel **(i)**.

SED
4, 1165–1204, 2012

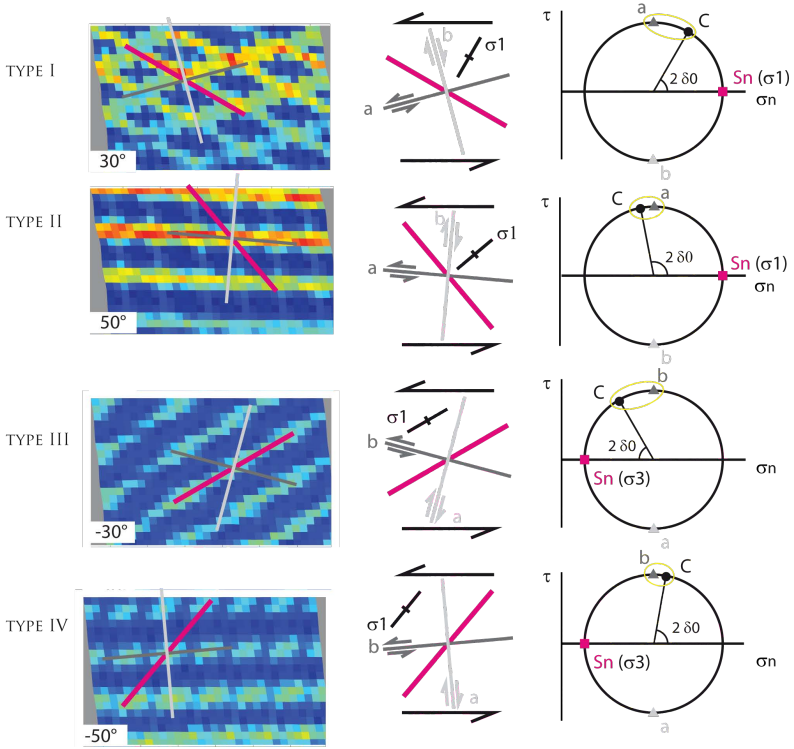

Fig. 9. Left column: finite strain at γ^{bulk} = 10 % with the Sn in purple line and the maximum shear stress directions (a and b) are reported in grey. Middle and Right columns: the black arrows represent the bulk simple shear imposed at the boundary and is represented as the black C dot on the Mohr circle. The cross indicates the local principal stress direction as deduced from the Mohr circle construction in the right column. The Sn is again reported as a purple line and represented by a purple square on the Mohr circle.

SED
4, 1165–1204, 2012

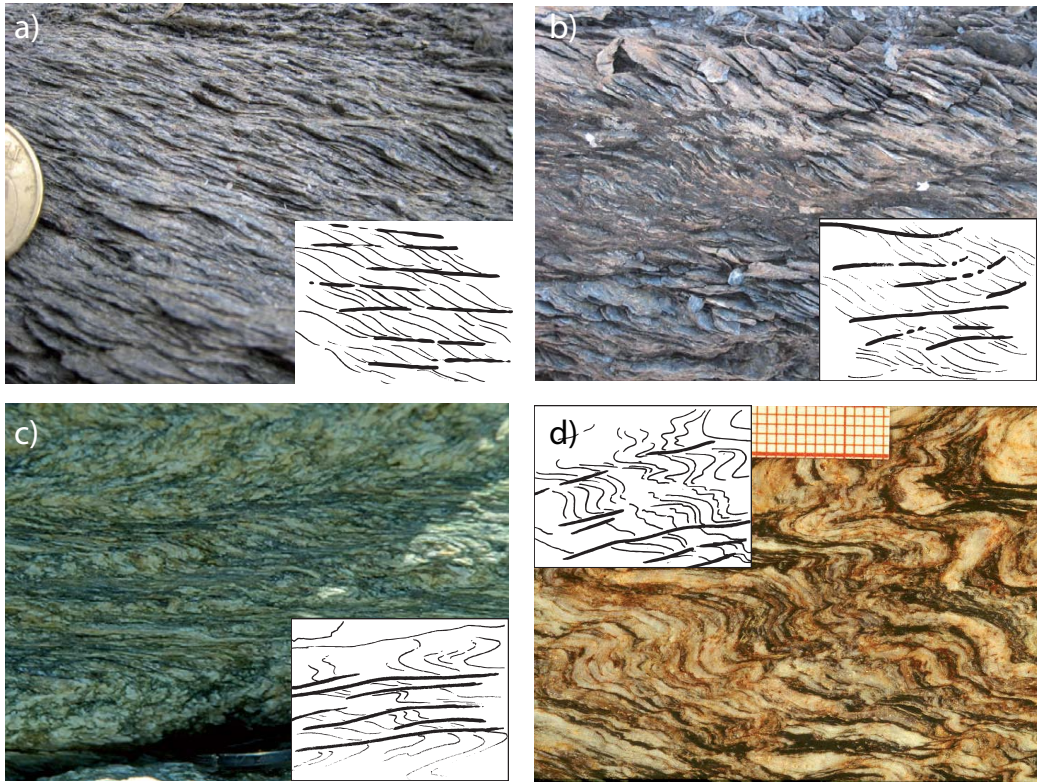

Fig. 10. Diversity of the microstructures in foliated media, **(a, b)** examples from Betics Spain **(c, d)** examples from Tende Corsica.

SED
4, 1165–1204, 2012